



## **Despeckling of Ultrasound Images Using Non-subsampled Shearlet Transform and Enhanced Gradient Domain Guided Filter**

**Rika Favoria Gusa<sup>1,2</sup>****Risanuri Hidayat<sup>1\*</sup>****Hanung Adi Nugroho<sup>1</sup>**<sup>1</sup>*Department of Electrical and Information Engineering, Universitas Gadjah Mada, Yogyakarta, Indonesia*<sup>2</sup>*Department of Electrical Engineering, Universitas Bangka Belitung, Indonesia*\* Corresponding author's Email: [risanuri@ugm.ac.id](mailto:risanuri@ugm.ac.id)

---

**Abstract:** Ultrasound imaging is widely used in medical diagnostics. However, the presence of speckle noise degrades image quality by reducing contrast and obscuring structural details. To overcome this problem, this study proposes a despeckling algorithm that integrates the non-subsampled shearlet transform, an enhanced gradient-domain guided filter (eGDGF) augmented with the maximum local variation (MLV) operator, and an improved thresholding shrinkage rule derived from the residual image weighted by a bilateral filter. The integration of the edge-aware eGDGF with the MLV operator enhances local contrast and structural sharpness in low-frequency subbands, while the improved thresholding shrinkage rule in high-frequency subbands enables adaptive speckle suppression and perceptual enhancement. Experimental results demonstrate that the proposed algorithm achieves effective noise reduction while preserving structural details and improving the perceptual quality of ultrasound images with varying noise levels.

**Keywords:** Ultrasound image, Speckle noise, Non-subsampled shearlet transform, Gradient domain guided filtering, Maximum local variation.

---

### **1. Introduction**

Ultrasound technology has been prevalent in medical imaging for decades. Compared to other imaging modalities, ultrasound possesses distinct beneficial characteristics. It is harmless as it does not involve ionizing radiation exposure and is non-invasive. Moreover, it is economically efficient and can produce real-time results [1, 2]. Ultrasound imaging uses sound waves with frequencies over 20 kHz. Ultrasound frequencies employed for clinical applications typically vary from 1 MHz to 12 MHz. Ultrasound waves originate from a transducer that transforms electrical energy into mechanical energy and operates based on the piezoelectric principle [3].

The physical interactions between ultrasound waves and tissues in the body fundamentally influence the quality of the generated ultrasound images. When ultrasound waves hit their target, they are reflected and interact in both destructive and constructive ways, resulting in speckles in the image. Speckle is an inherent multiplicative noise that

obscures the image edges. Furthermore, slight variations in the number of reflected ultrasound waves, caused by subtle variances in the acoustic impedance of tissues in the body, typically result in ultrasound images with low contrast. The presence of speckle noise exacerbates this lack of contrast. Consequently, suppressing speckle noise prior to the analysis and processing of ultrasound images is essential, and a significant number of researchers have concentrated their efforts on this matter [4, 5].

Denosing techniques applicable to medical ultrasound images can be classified into three categories: spatial domain filters, transform domain filters, and hybrid filters [6]. Some common spatial domain filters, like median filter [7, 8] bilateral filter [9, 10] and guided filter (GF) [11], reduce image noise by utilizing the statistical characteristics of neighboring pixels in a specified local window. The reduction of speckle noise mainly depends on the local window size. Moreover, there are fundamental trade-offs present between noise suppression and

edge preservation, which frequently result in the blurring of details.

Another type of spatial filter is the speckle reducing anisotropic diffusion (SRAD) filter and its derivatives, such as the modified SRAD (MSRAD) filter and the detail preserving anisotropic diffusion filter. Anisotropic diffusion filters reduce diffusivity at edge locations and facilitate diffusion in homogeneous regions with small intensity changes [12]. These filters effectively diminish speckle noise and maintaining critical edges and features in the image, but they need extensive computing time and rely significantly on parameter selection.

Wavelet, contourlet, and shearlet are some transform domain denoising techniques. The wavelet transform suppresses noise by decomposing the noisy image into one low-frequency (LF) subband and three high-frequency (HF) subbands and then applying thresholding to the coefficients in the HF subbands [13]. By integrating the Laplacian pyramid and directional filter bank, the contourlet transform effectively captures geometric information while removing noise in the image [14].

The shearlet transform offers more flexibility in representing the geometric structure of images [15]. To address the issue of shift invariance in contourlet and shearlet transforms, the nonsubsampling contourlet transform (NSCT) and nonsubsampling shearlet transform (NSST), respectively, were introduced by removing subsampling procedures at each decomposition step [14, 16]. Although transform-domain filters are proficient at differentiating noise from structural elements, they frequently exhibit sensitivity to direction or shifts. Their effectiveness is significantly influenced by the selected threshold rule, which limits their adaptability to spatially varying noise, such as speckle in ultrasound images.

A number of studies have suggested combining transform-domain with spatial-domain filters to further enhance denoising performance. A homomorphic NSCT employing a thresholding function, a bilateral filter, and a self-organizing map (SOM) was proposed to despeckle ultrasound images [17]. The technique demonstrates excellent denoising performance, as evidenced by increased peak signal-to-noise ratio (PSNR) and structural similarity index (SSIM) following the SOM-based deblurring stage. Ilesanmi et al. [18] combined the Wiener filter and the new fast bilateral filter to eliminate speckle noise. Meanwhile, artifacts in the image were removed using a combination of wavelet and anisotropic filters. This approach effectively reduces speckle but induces visual blurriness.

The NSCT was combined with a cross-guided bilateral filter to improve the quality of ultrasound images through despeckling [19]. This method simplifies the process of filtering speckle noise, although its effectiveness diminishes in the presence of high noise levels. Jubairahmed et al. [20] combined the contourlet transform with an SRAD filter in the HF subbands and adaptive thresholding in the LF subband. Their findings indicate that the proposed method substantially eliminates speckle noise in ultrasound images but also decreases edge sharpness. A technique based on the NSST and a GF was used for despeckling ultrasound images [21]. An enhanced threshold function and a three-variable shrinkage function were introduced to execute thresholding in the HF subbands. Meanwhile, the GF processed the LF subbands. This technique is effective in filtering speckle noise. Bedi et al. [22] applied the NSST to remove speckle noise and enhance ultrasound images. They used MSRAD in the LF subband. Their approach preserves structures and edges and enhances contrast but requires more computational time.

In recent years, developments in image denoising have shown an increasing focus on integrating multiscale transform representations with data-driven learning models to improve speckle suppression and detail preservation. Lyu et al. [23] introduced NSTBNet, a hybrid framework that combines the NSST with a broad convolutional neural network (CNN) architecture to enhance texture reconstruction and increase robustness to Gaussian noise in images. Similarly, Katta et al. [24] proposed a dual-phase denoising strategy that combines the NSST with Bayesian thresholding and integrates a method-noise Deep CNN-based post-processing operation for CT image enhancement, showcasing significant advancements in visual quality when compared to conventional filters. The findings highlight the efficacy of hybrid NSST–CNN methods, with transform-domain decomposition offering directional sparsity and CNN-based learning improving non-linear feature extraction.

Parallel to these hybrid models, recent research has also explored frameworks that rely solely on deep learning techniques functioning entirely within the spatial domain. Sun et al. [25] presented NSBR-Net, a transformer-based segmentation model that incorporates a noise suppression module (NSM) and a boundary refinement module (BRM). This model effectively decouples high- and low-frequency components to reduce speckle interference and enhance the precision of lesion boundaries. Kang et al. [26] introduced a residual network (ResNet) model tailored for ultrasound image denoising,

demonstrating notable improvements in PSNR and RMSE when compared to traditional spatial filters like median and Wiener filters.

Khalifa et al. [27] introduced a metric-optimized knowledge distillation (MK) model designed to facilitate the transfer of knowledge from a high-capacity teacher network to a lightweight student model, achieving an effective balance between denoising accuracy and computational efficiency. Yu et al. [28] introduced a self-supervised ultrasound denoising framework that combines a blind-neighborhood network (BNN) and U-Net using a weighted joint loss function. This approach removes the requirement for clean–noisy image pairs while effectively balancing noise removal with structural fidelity. The performance of these data-driven methods is remarkable; however, they often depend on large annotated datasets, significant GPU resources, and prolonged training duration, which can limit their application in resource-constrained settings.

According to the previously discussed literature, existing ultrasound despeckling techniques reveal various limitations, even with notable advancements. Conventional spatial-domain filters frequently lead to significant smoothing and edge blurring as a result of their dependence on local averaging. Transform-domain methods, such as those utilizing the NSST, successfully distinguish between high- and low-frequency components; however, they can still result in ringing artifacts or a reduction in texture detail when fixed thresholding rules are employed. Deep learning frameworks, despite their capabilities, necessitate extensive annotated datasets and demand significant computational resources. As a result, there is an essential requirement for an approach that does not rely on training and can efficiently reduce speckle noise while preserving structural integrity, offering an alternative to data-intensive deep learning paradigms.

To address these challenges, this study proposes a new ultrasound image despeckling algorithm designed to enhance image quality without compromising structural fidelity. The proposed framework integrates the NSST, an enhanced gradient domain guided filter (eGDGF), and an improved thresholding function. The NSST decomposes the input image into low-frequency (LF) and high-frequency (HF) subbands, enabling scale-adaptive processing. The eGDGF, augmented with the maximum local variation (MLV) operator, is applied to the LF subband to improve edge preservation while maintaining natural brightness and local contrast. Meanwhile, the improved thresholding function—constructed on the Bayesian

shrinkage rule and a bilateral filter—enhances the adaptability of HF denoising, allowing for more effective speckle suppression while retaining fine perceptual details. This integrated design allows the algorithm to effectively suppress speckle noise while preserving both structural and perceptual fidelity.

The remainder of this paper is organized as follows. Section 2 presents the research methods, including the theoretical background of the algorithmic components, the overall research framework, and the mathematical expressions used for performance evaluation. Section 3 provides the experimental results and detailed discussions of the findings. Finally, Section 4 concludes the paper by summarizing the main contributions.

## 2. Methods

The proposed ultrasound image despeckling algorithm comprises three key components: the NSST, the GDGF, and a thresholding function.

### 2.1 Non-sampled shearlet transform

The shearlet transform was developed to address the directionality and anisotropy constraints presented by the wavelet transform when applied to

Table 1. Notation list

Symbol	Description
$A_{AB}$	Shearlet basis function system
$\psi$	Basis function
$A$	Anisotropic matrix
$B$	Multi-orientation shearing matrix
$j$	Number of scaling operations
$l$	Number of direction operations
$k$	Shift parameter
$J$	Number of decomposition level
$a_{p'}, b_{p'}$	Linear coefficients of GDGF
$Z$	Local output image of GDGF
$X$	Input (noisy) image
$G$	Guidance image
$\Omega_r$	Local window (radius $r$ )
$\lambda$	Regularization parameter
$\hat{\Gamma}_G$	Edge-aware weight
$N$	Number of image pixels
$L$	Dynamic range
$H$	Enhanced image
$T$	Threshold
$q$	Total number of subband coefficients
$r_k$	Residual image
$x_k$	Speckled image
$s_k$	Despeckled image
$f_1, f_2$	Optimized weights
$\nabla(u, v)$	MLV at pixel $(u, v)$
$s$	Noise-free image

multidimensional functions. The shearlet transform provides a superior and more detailed way to represent an image due to its significant directional sensitivity and optimal sparsity [29]. The shearlet basis function system in dimension  $n = 2$  is shown in Eq. (1).

$$A_{AB}(\psi) = \left\{ \psi_{j,l,k}(x) = |\det A|^{\frac{j}{2}} \psi(B^l A^j(x-k)) : j, l \in \mathbb{Z}, k \in \mathbb{Z}^2 \right\} \quad (1)$$

where  $\psi \in L^2(\mathbb{R}^2)$  denotes a basis function,  $A$  signifies an invertible anisotropic matrix for scale operation,  $B$  represents an invertible multi-orientation shearing matrix, and  $j$  and  $l$  determine the number of scaling and direction operations on the basis functions, whereas  $k$  is the shift parameter that signifies location. Parameters  $A = A_d$  and  $B = B_d$  for  $d = 0, 1$  are as follows:

$$\begin{aligned} A_0 &= \begin{bmatrix} 4 & 0 \\ 0 & 2 \end{bmatrix}, B_0 = \begin{bmatrix} 1 & 1 \\ 0 & 1 \end{bmatrix}, \\ A_1 &= \begin{bmatrix} 2 & 0 \\ 0 & 4 \end{bmatrix}, B_1 = \begin{bmatrix} 1 & 0 \\ 1 & 1 \end{bmatrix}. \end{aligned} \quad (2)$$

The shearlet transform fails to address the shift-invariance issue introduced by the downsampling and upsampling processes in the algorithm. By omitting the downsampling and upsampling procedures on the Laplacian pyramid, the NSST becomes a shift-invariant type of shearlet transform. The NSST discretization technique consists of two phases: multiscale decomposition, accomplished by a non-subsampled Laplacian pyramid (NSLP) filter bank, and orientation localization, performed with a shearlet filter (SF) [30].

The NSLP divides the input image into a HF subband and an LF subband at the first decomposition stage. At higher stages, the LF subband undergoes decomposition to produce both HF and LF subbands. The filter utilized for the higher levels of the decomposition process is derived by upsampling the filter from the first level. When the decomposition level is established at  $J$ , the input image is partitioned into  $J+1$  subbands of identical dimensions to the input image, one of which is an LF subband. To achieve orientation localization, the SF is used to create  $2^l$  directional subbands for each HF subband, and these subbands are the same size as the input image.

## 2.2 Gradient domain guided filter

The objective of gradient domain guided filtering (GDGF) is to determine the linear coefficients  $a_{p'}$  and  $b_{p'}$  to produce the local output image  $Z_p$  according to

Eq. (3) by minimizing the local cost function in Eq. (4) [31].

$$Z_p = a_{p'} G_p + b_{p'}, \forall p \in \Omega_r(p') \quad (3)$$

$$\sum_{p \in \Omega_r(p')} [(a_{p'} G_p + b_{p'} - X_p)^2 + \frac{\lambda}{\hat{\Gamma}_G(p')} (a_{p'} - \gamma_{p'})^2] \quad (4)$$

$X_p$  represent the input image in the local window  $\Omega_r(p')$ , while  $G_p$  represents the guidance image in the same window, both centered at  $p'$  with a radius  $r$ .  $\lambda$  serves as the regularization parameter to avoid  $a_{p'}$  from becoming excessively large.

$\hat{\Gamma}_G(p')$  is an edge-aware weight which is defined by using Eq. (5).

$$\hat{\Gamma}_G(p') = \frac{1}{N} \sum_{p=1}^N \frac{\chi(p)+\varepsilon}{\chi(p)+\varepsilon} \quad (5)$$

$$\chi(p') = \sigma_{G,1}(p') \sigma_{G,r}(p') \quad (6)$$

where  $N$  is the number of image pixels.  $\varepsilon$  is a constant, determined as  $(0.001 \times L)^2$ , where  $L$  is the dynamic range of the input image. To generally define the function  $\chi(\cdot)$ ,  $\chi(p')$  as in Eq. (6) is used.  $\sigma_{G,1}(p')$  and  $\sigma_{G,r}(p')$  are the standard deviation of the  $3 \times 3$  window and  $(2r+1) \times (2r+1)$  window, respectively.

Parameter  $\gamma_{p'}$  is presented in Eq. (7).

$$\gamma_{p'} = 1 - \frac{1}{1 + e^{\eta(\chi(p') - \mu_{\chi,\infty})}} \quad (7)$$

where  $\mu_{\chi,\infty}$  indicates the mean value of the dataset  $\{\chi(p) | \forall p \in \Omega_r(p')\}$  and

$$\eta = \frac{4}{\mu_{\chi,\infty} - \min(\chi(p), \forall p \in \Omega_r(p'))} \quad (8)$$

The prime values of  $a_{p'}$  and  $b_{p'}$  are calculated according to Eq. (9).

$$\begin{aligned} a_{p'} &= \frac{\mu_{G \otimes X, r}(p') - \mu_{G, r}(p') \mu_{X, r}(p') + \frac{\lambda}{\hat{\Gamma}_G(p')} \gamma_{p'}}{\sigma_{G, r}^2(p') + \frac{\lambda}{\hat{\Gamma}_G(p')}} \\ b_{p'} &= \mu_{X, r}(p') - a_{p'} \mu_{G, r}(p') \end{aligned} \quad (9)$$

Then, the value of  $Z_p$  is presented as follows:

$$Z_p = \bar{a}_p G_p + \bar{b}_p \quad (10)$$

where  $\bar{a}_p$  and  $\bar{b}_p$  are the mean values of  $a_{p'}$  and  $b_{p'}$  in the window  $\Omega_r(p')$ , respectively.

The image is smoothed while the detailed features are preserved through GDGF. The edge and detail of

the image can be enhanced by subtracting the filtered image from the original image, resulting in a difference image. The difference image is subsequently combined with the filtered image to yield an enhanced version [32]. The formula is outlined below.

$$H_p = Z_p + c(X_p - Z_p) \quad (11)$$

where  $c$  is the scale coefficient.

### 2.3 Thresholding function

Thresholding functions can be categorized into two primary types: hard thresholding (HT), in which each value is assessed in comparison to a defined threshold and any value lower than this threshold is changed with a value of zero, and soft thresholding (ST), where coefficients exceeding the threshold are adjusted by subtracting the threshold from them. ST produces more visually appealing images than HT, as the latter tends to be discontinuous and results in abrupt artifacts in the restored images, particularly when the noise energy is substantial. The ST function is defined as follows:

$$s_T(x) = \text{sgn}(x) \cdot \max(|x| - T, 0) \quad (12)$$

where  $T$  is the threshold.

The Bayesian shrinkage rule, proposed by Chang et al. [33], is a technique that suggests an adaptively determined threshold based on the value of the coefficients in each detail (HF) subband. The threshold is calculated using Eq. (13).

$$T = \frac{\sigma_n^2}{\sigma_y} \quad (13)$$

where  $\sigma_n^2$  is the noise variance and  $\sigma_y$  is the standard deviation of the original image.

A robust median estimator is employed to estimate the noise variance ( $\sigma_n^2$ ) from the HF subband at the first level of decomposition of the noisy image ( $X_I(u,v)$ ).

$$\sigma_n^2 = \left[ \frac{\text{median}(|X_I(u,v)|)}{0.6745} \right]^2 \quad (14)$$

The variance of a noisy image ( $\sigma_x^2$ ) can be expressed using the following equation:

$$\sigma_x^2 = \sigma_y^2 + \sigma_n^2 \quad (15)$$

Therefore, Eq. (16) can be used to calculate  $\sigma_y$ .

$$\sigma_y = \sqrt{\max(\sigma_x^2 - \sigma_n^2, 0)} \quad (16)$$

$$\sigma_x^2 = \frac{1}{q} \sum_{i=1}^q X_i^2 \quad (17)$$

where  $q$  is the total number of subband coefficients of the noisy image  $X$ .

The Bayesian shrinkage rule is further enhanced by employing the residual image with bilateral filtering [17]. The residual image ( $r_k$ ) can be denoted as follows:

$$r_k = x_k - s_k \quad (18)$$

where  $x_k$  and  $s_k$  are the speckled image and the despeckled image, respectively. Eq. (18) can be expressed in another form as follows:

$$\theta(x_k) = f_1 s_k + f_2 r_k \quad (19)$$

where  $f_1$  and  $f_2$  represent the optimized weights aimed at achieving optimal results.

Once the value of  $r_k$  from Eq. (18) is substituted into Eq. (19), Eq. (20) can be written as follows:

$$\theta(x_k) = (f_1 - f_2) s_k + f_2 x_k \quad (20)$$

Let  $g_1 = (f_1 - f_2)$ ,  $g_2 = f_2$ ,  $s_{k1} = s_k$ , and  $s_{k2} = x_k$ . Hence, Eq. (20) will be reformulated as Eq. (21) below.

$$\theta(x_k) = g_1 s_{k1} + g_2 s_{k2} \quad (21)$$

where  $g_1$  and  $g_2$  should be linear.

The weight values,  $g_1$  and  $g_2$ , are determined by assessing spatial proximity and variations in intensity values. Consider the pixel at  $(u_1, v_1)$  be required to despeckle its surrounding pixels, one of which is located at  $(u_2, v_2)$ . Consequently, the weight value can be approximated utilizing the range and Gaussian kernels as demonstrated in Eq. (22).

$$g = \exp \left( - \frac{(u_1 - u_2)^2 + (v_1 - v_2)^2}{2\sigma_d^2} - \frac{\|x_k(u_1, v_1) - x_k(u_2, v_2)\|^2}{2\sigma_r^2} \right) \quad (22)$$

where  $\sigma_d$  is the spatial standard deviation,  $\sigma_r$  is the range standard deviation, and  $x_k(u_1, v_1)$  and  $x_k(u_2, v_2)$  are the pixel intensities at  $(u_1, v_1)$  and  $(u_2, v_2)$  respectively.

A new thresholding shrinkage rule, as determined in Eq. (23), is suggested based on the linear function outlined in Eq. (20) [17].

$$\theta(x_k) = \begin{cases} 0 & \text{if } \theta(x_k) < 0 \\ \theta(x_k) & \text{Otherwise} \end{cases} \quad (23)$$

### 2.4 Proposed algorithm

The overall workflow of the proposed ultrasound image despeckling algorithm is illustrated in Fig. 1. In this study, 130 images were randomly selected from three publicly available and clinically validated datasets: the Digital Database for Thyroid Images (DDTI) [34], the Breast Ultrasound Images Dataset [35], and the Maternal–Fetal Ultrasound Dataset [36]. These datasets encompass diverse imaging systems and various noise levels. The tested images have spatial resolutions ranging from  $560 \times 360$  to  $1495 \times 787$  pixels. All datasets were curated and annotated by certified medical experts. To preprocess the input, a logarithmic transform was applied to convert the multiplicative characteristics of speckle noise into an additive form. Afterward, the NSLP was employed with three decomposition levels and eight shearing directions per level, producing one low-frequency (LF) subband and three high-frequency (HF) subbands.

The GDGF was used to suppress noise in the LF subband. It was selected due to its exceptional edge-preserving capabilities, which make it highly appropriate for the LF subband that stores the global structure of the image. Additionally, the GDGF has low computational complexity. We used the LF image as both the guidance image and the input image for the GDGF. This was done with the assumption that most of the noise has been handled in the HF subbands. The radius ( $r$ ) of the local window in the GDGF was set at 10, as finer features in the image are effectively retained at this value, whereas they begin

to blur when  $r$  exceeds 10. Meanwhile, the regularization parameter ( $\lambda$ ) was set to 0.05. This value was chosen as a moderate option because it does not significantly affect image quality. To improve the detailed features in the output image of the GDGF, the difference image and the scale coefficient are required as per Eq. (11). The difference image was derived by subtracting the output image of the GDGF (filtered LF image) from the input (LF) image. The MLV operator was added to measure the maximum change in the local region of the input image, thereby enhancing the image’s contrast and sharpening the local details without amplifying the noise or changing the mean brightness level.

The MLV was determined by calculating the variation between the value of a center pixel inside the local region and its eight adjacent pixels as described in Eq. (24). The normalized maximum value of these variations serves as the weight for the difference image. Therefore, we proposed a new enhanced version of gradient domain guided filtering as outlined in Eq. (25).

$$\nabla(u,v) = \max \{ |X(u-1, v-1) - X(u,v)|, |X(u-1, v) - X(u,v)|, |X(u-1, v+1) - X(u,v)|, |X(u, v-1) - X(u,v)|, |X(u, v+1) - X(u,v)|, |X(u+1, v-1) - X(u,v)|, |X(u+1, v) - X(u,v)|, |X(u+1, v+1) - X(u,v)| \} \quad (24)$$

$$H_p = Z_p + c \nabla(u,v) (X_p - Z_p) \quad (25)$$

where  $\nabla(u,v)$  is the MLV at pixel  $(u,v)$ .

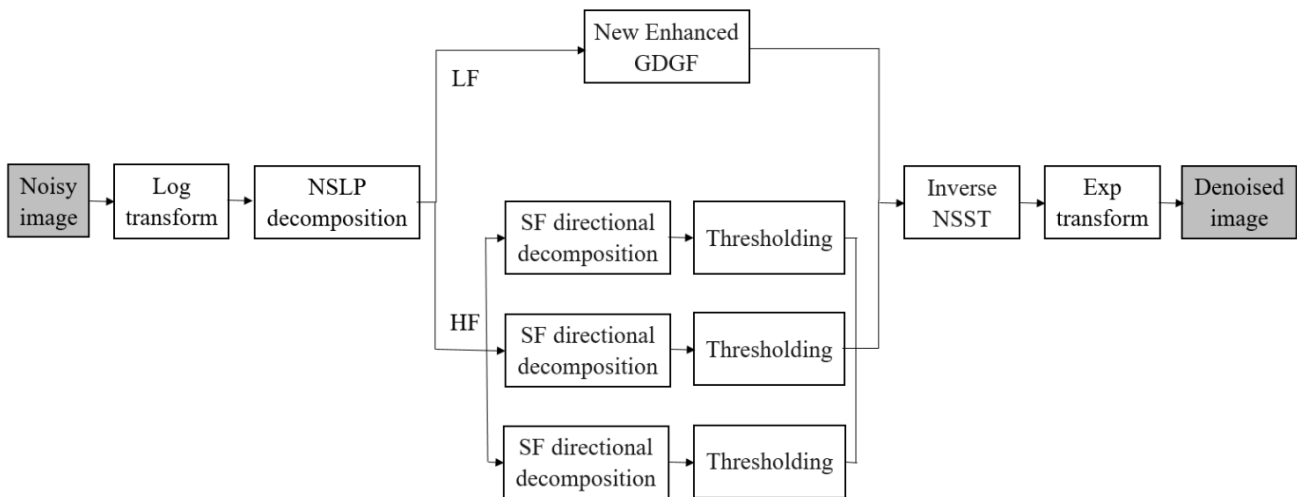


Figure. 1 The proposed ultrasound image despeckling algorithm

To reduce noise in the HF subbands, soft thresholding with a threshold value determined by the Bayesian shrinkage rule was employed. The residual image with a bilateral filter approach was used to improve the Bayesian shrinkage rule. The local regions in the HF images were weighted according to their spatial proximity and intensity value differences. To calculate the weight values using Eq. (22), we assigned the spatial standard deviation ( $\sigma_d$ ) a value of 2, while  $\sigma_r$  was determined based on the local variance of the image. The weight values were subsequently applied in Eq. (21). The results of the thresholding process in the HF subbands were derived using Eq. (23). Furthermore, the inverse NSST was applied, followed by exponential transform, to obtain a despeckled image.

The effectiveness of the proposed method was evaluated in comparison with several NSST-based approaches, including NSST with a weighted bilateral filter (WBF) and hard thresholding [16], NSST with a GF and an improved threshold function [21], NSST with MSRAD and hard thresholding [22], and NSST with enhanced GDGF [37]. Quantitative evaluation metrics were employed to assess the performance of the proposed method. The metrics included equivalent number of looks (ENL), mean preservation speckle suppression index (MPSSI), edge preservation index (EPI), average gradient (AG), average local contrast (ALC), and natural image quality evaluator (NIQE).

## 2.5 Performance evaluation of image despeckling techniques

### 2.5.1. Equivalent number of looks

ENL serves as a quantitative measure of the level of noise present in an image.

$$ENL = \frac{\text{mean}(F)^2}{\text{var}(F)} = \frac{\bar{F}^2}{\sigma_F^2} \quad (26)$$

where  $F$  is the filtered image. An increase in the ENL value of the filter correlates with enhanced efficiency in elevating the signal to noise ratio (SNR) within a homogeneous region [38].

### 2.5.2. Mean preservation speckle suppression index

The MPSSI is defined as follows:

$$MPSSI = \left| 1 - \frac{\mu_F}{\mu_M} \right| \cdot \frac{\sigma_F}{\sigma_M} \quad (27)$$

where  $\mu_F$  and  $\mu_M$  represent the mean values, whereas  $\sigma_F$  and  $\sigma_M$  denote the standard deviations of filtered

image and speckled image, respectively. Lower MPSSI values signify enhanced filter performance on mean preservation and noise reduction, regardless of the actual mean value [38].

### 2.5.3. Edge preservation index

The capacity of image denoising techniques to preserve the edges of objects in the image is calculated using Eq. (28).

$$EPI = \frac{\Gamma(\Delta s - \overline{\Delta s}, \widehat{\Delta s} - \overline{\widehat{\Delta s}})}{\sqrt{\Gamma(\Delta s - \overline{\Delta s}, \Delta s - \overline{\Delta s}) \cdot \Gamma(\widehat{\Delta s} - \overline{\widehat{\Delta s}}, \widehat{\Delta s} - \overline{\widehat{\Delta s}})}} \quad (28)$$

where  $s$  represents the noise-free image,  $\hat{s}$  denotes the denoised image, and  $\Delta s$  and  $\widehat{\Delta s}$  are the HF filtered versions of  $s$  and  $\hat{s}$ , respectively, which are obtained through the application of the Laplacian operator [39].

### 2.5.4. Average gradient

AG denotes the degree of sharpness and clarity, which can be assessed using Eq. (29).

$$AG = \frac{\sum_i \sum_j ((f(u,v) - f(u+1,v))^2 + (f(u,v) - f(u,v+1))^2)^{\frac{1}{2}}}{mn} \quad (29)$$

where  $f(u,v)$  is the pixel intensity, and  $m$  and  $n$  represent the number of rows and columns in the image, respectively [40].

### 2.5.5. Average local contrast

The ALC is derived by computing the mean of the local contrast, defined as follows:

$$ALC = \frac{\delta_w^2}{\mu_w} \quad (30)$$

where  $\delta_w^2$  represents the local variance of intensity and  $\mu_w$  denotes the local mean of intensity [40].

### 2.5.6. Natural image quality evaluator

NIQE assesses the quality of an image without a reference by contrasting it with a standard model derived from images depicting natural scenes that exhibit minimal or no noticeable distortion. A lower score signifies enhanced perceptual quality [41].

## 3. Results and discussion

In this work, the NSST with a new enhanced GDGF and bilateral filtering-based modified thresholding (NSST+eGDGF+MLV) was applied to

medical ultrasound images. The performance of the method was compared to several NSST-based approaches to ensure a fair and consistent performance comparison under similar processing conditions. The comparative methods included NSST with a WBF and hard thresholding (NSST+WBF) [16], NSST with a GF and an improved threshold function (NSST+GF) [21], NSST with MSRAD and hard thresholding (NSST+MSRAD) [22], and NSST with enhanced GDGF (NSST+eGDGF) [37]. We also compared the proposed method to the NSST with an enhanced GDGF without adding the MLV operator (NSST+eGDGF). Fig. 2 and Table 2 display the results of the despeckling process on a thyroid ultrasound image.

Fig. 2(a) shows a noisy thyroid ultrasound image with an AG value of 16.9510 and an ALC value of 2.6023. Fig. 2(b) and Table 2 show that NSST+WBF mitigated speckle noise effectively. This performance is reflected by its high ENL value of 3.583. The homogeneous areas in Fig. 2(b) exhibit a degree of smoothness, although some residual noise is still perceptible. NSST+WBF attained the lowest MPSSI value of 0.002, indicating excellent mean preservation. A high EPI value of 0.954 signifies that the edges remain preserved with no new edges introduced. The elevated AG and ALC values, 14.835 and 2.091, respectively, suggest that the image exhibits commendable sharpness and contrast. However, they also imply the presence of some residual noise. The poor NIQE score of 15.563 is due to textures that appear unnatural to human vision.

NSST+GF demonstrated a significant reduction in speckle noise, as illustrated in Fig. 2(c), alongside the highest ENL value of 4.704 presented in Table 2. Nonetheless, this method resulted in image blurring due to over-smoothing, as evidenced by the lowest AG and ALC values of 5.738 and 0.347, respectively. The NIQE score of 10.824 is poor due to excessive smoothness in the image. However, the outlines of important structures are still apparent, leading to an elevated EPI value of 0.941. The mean preservation is also quite satisfactory, resulting in a relatively low MPSSI value of 0.009.

NSST+MSRAD exhibited suboptimal speckle reduction, as shown in Fig. 2(d) and by its low ENL value of 2.607 in Table 2. It also introduced a

noticeable brightness alteration, resulting in an MPSSI score of 14.844, which is the poorest among all methods evaluated. Nevertheless, the despeckled image exhibits strong contrast and sharpness, as indicated by the AG and ALC values of 34.775 and 3.488, respectively. Additionally, it presents a smooth appearance, as demonstrated by its comparatively low NIQE score of 8.637. The edge quality is maintained at an excellent level, with NSST+MSRAD reaching the highest EPI value of 0.984.

NSST+eGDGF produced a despeckled image, as shown in Fig. 2(e). This image exhibits significant changes in the mean of pixel intensities, as indicated by the MPSSI value of 0.016 in Table 2. The homogenous regions demonstrate inadequate cleanliness due to speckle noise, with a granular

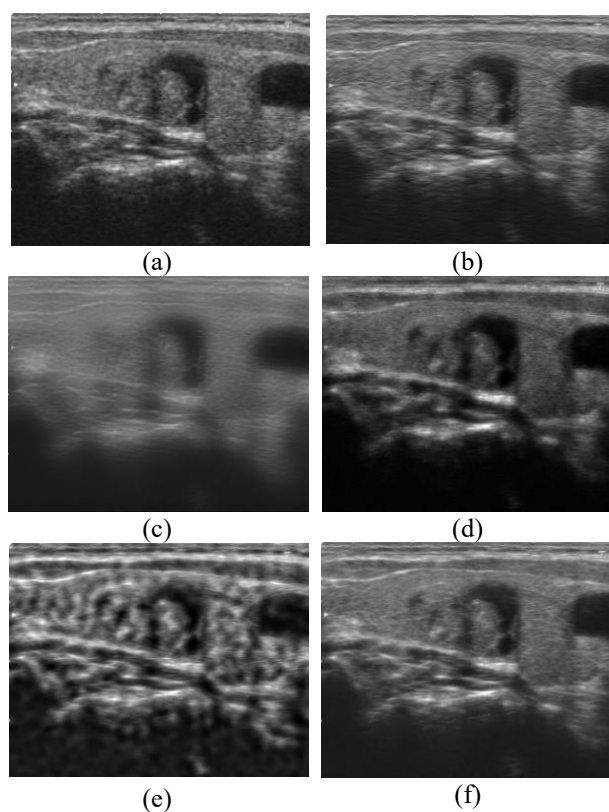


Figure. 2 The results of the despeckling of a thyroid ultrasound image: (a) Noisy image, (b) NSST+WBF [17], (c) NSST+GF [22], (d) NSST+MSRAD [23], (e) NSST+eGDGF [37], and (f) NSST+eGDGF+MLV

Table 2. Comparison of the despeckling performance of different methods applied to a thyroid ultrasound image

Method	ENL ( $\uparrow$ )	MPSSI ( $\downarrow$ )	EPI ( $\uparrow$ )	AG ( $\uparrow$ )	ALC ( $\uparrow$ )	NIQE ( $\downarrow$ )
NSST+WBF	3.583	<b>0.002</b>	0.954	14.835	2.091	15.563
NSST+GF	<b>4.704</b>	0.009	0.941	5.738	0.347	10.824
NSST+MSRAD	2.607	14.844	<b>0.984</b>	<b>34.775</b>	<b>3.488</b>	8.637
NSST+eGDGF	2.479	0.016	0.937	11.602	1.674	9.032
NSST+eGDGF+MLV	3.489	0.003	0.942	9.992	1.234	<b>8.477</b>

texture still being prominent. The lowest ENL value of 2.479 also indicates this. The remaining noise leads to elevated AG and ALC values of 11.602 and 1.674, respectively. The presence of unwanted edges deteriorates the texture and results in the lowest EPI value of 0.937. A relatively high NIQE value of 9.032 indicates poor perceptual quality.

NSST+eGDGF+MLV effectively reduced speckle noise while maintaining edges and fine details, as demonstrated in Fig. 2(f). The elevated ENL value of 3.489 presented in Table 2 proves this assertion. The EPI remains high at 0.942, confirming that edge quality is well preserved, although noise suppression causes a slight weakening of edge strength. Simultaneously, this method preserved the average of pixel intensities, resulting in a favorable MPSSI of 0.003. It also provided good contrast and sharpness, as demonstrated by its AG and ALC values. The despeckled image exhibits a smooth, visually pleasing texture, as evidenced by the best NIQE score of 8.477.

Fig. 3(a) shows a noisy breast ultrasound image with an AG value of 6.8682 and an ALC value of 0.4971. In Fig. 3(b), residual noise remains perceptible because the speckle noise reduction by NSST+WBF is inadequate. Fig. 3(c) shows that speckle noise is successfully removed by NSST+GF; however, the image becomes blurry due to over-smoothing. NSST+MSRAD demonstrates significant efficacy in reducing speckle noise, resulting in a clear image with enhanced contrast, as observed in Fig. 3(d). The despeckled image in Fig. 3(e), produced using NSST+eGDGF, exhibits strong contrast. Nevertheless, it is affected by considerable residual noise and diminished perceptual quality. Meanwhile, Fig. 3(f) illustrates the effectiveness of NSST+eGDGF+MLV in eliminating speckle noise and keeping edges and fine details while also providing excellent contrast.

Table 3 provides more details on the performance of the despeckling methods used to generate the images in Fig. 3. NSST+WBF produced an image with the lowest MPSSI value of 0.001. This results from minimal change in average pixel intensity compared to the input image. Important structures and image sharpness are preserved, as indicated by

the high EPI, AG, and ALC values of 0.953, 6.153, and 0.428, respectively. Nevertheless, high AG and ALC values may also result from residual noise. The presence of residual noise leads to poor perceptual quality, as indicated by the highest NIQE value of 8.730.

NSST+GF exhibited remarkable noise reduction. This is evidenced by the highest ENL value of 2.351. However, the despeckled image displays a lack of clarity due to excessive smoothing.

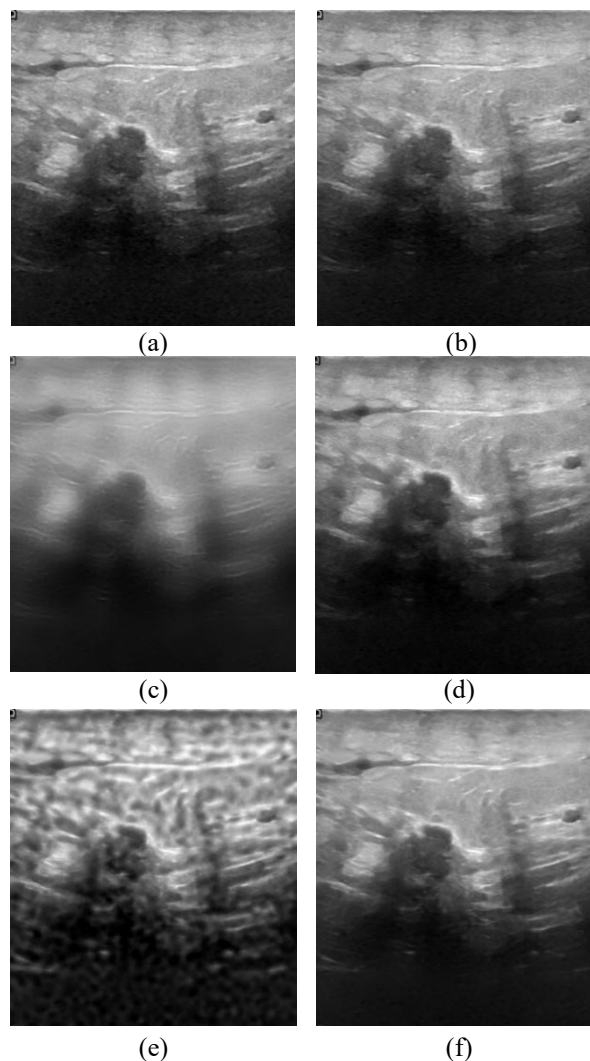


Figure 3 The results of the despeckling of a breast ultrasound image: (a) Noisy image, (b) NSST+WBF [17], (c) NSST+GF [22], (d) NSST+MSRAD [23], (e) NSST+eGDGF [37], and (f) NSST+eGDGF+MLV

Table 3. Comparison of the despeckling performance of different methods applied to a breast ultrasound image

Method	ENL (↑)	MPSSI (↓)	EPI (↑)	AG (↑)	ALC (↑)	NIQE (↓)
NSST+WBF	2.238	<b>0.001</b>	0.953	6.153	0.428	8.730
NSST+GF	<b>2.351</b>	0.003	0.897	2.536	0.084	6.772
NSST+MSRAD	1.995	2.324	<b>0.994</b>	<b>9.470</b>	<b>0.512</b>	5.786
NSST+eGDGF	2.037	0.005	0.884	6.039	0.489	6.401
NSST+eGDGF+MLV	2.242	0.001	0.894	4.442	0.310	<b>5.746</b>

This leads to reduced sharpness and contrast, as indicated by the lowest AG and ALC values of 2.536 and 0.084, respectively. Fig. 3(d) highlights the notable speckle reduction by NSST+MSRAD. The preservation of important structures is remarkable, as indicated by the highest EPI value of 0.994. Image contrast and sharpness are excellent, as indicated by the highest AG and ALC values of 9.470 and 0.512, respectively. Nevertheless, the enhancement of contrast levels results in higher variance. This leads to the lowest ENL value of 1.995 and the poorest MPSSI value of 2.324.

Based on Table 3, NSST+eGDGF shows limited speckle suppression with a low ENL of 2.037, despite good contrast and sharpness (AG = 6.039, ALC = 0.489) that also indicate residual noise. The low EPI value of 0.884 suggests additional edges in the despeckled image. In contrast, NSST+eGDGF+MLV effectively removes speckle noise with a higher ENL of 2.242 while maintaining acceptable contrast, sharpness, and detail (AG = 4.442, ALC = 0.310, EPI = 0.894), achieving excellent visual quality with a NIQE value of 5.746.

Fig. 4 and Table 4 display the results of applying various despeckling methods to a fetal brain ultrasound image. Fig. 4(a) shows a noisy fetal brain ultrasound image with an AG value of 5.4136 and an ALC value of 2.5472. The despeckled image in Fig. 4(b) achieves the lowest MPSSI value of 0.003 and a high EPI value of 0.999. These values demonstrate the effectiveness of NSST+WBF in maintaining both the average pixel intensity and important structures from the input (noisy) image. Elevated AG and ALC values of 5.258 and 2.369, respectively, indicate the presence of residual noise. It negatively affects visual quality, as confirmed by a poor NIQE value of 4.163. Despite this, NSST+WBF provides a favorable ENL value of 0.782, reflecting low variance and minimal pixel fluctuation in homogeneous regions. Meanwhile, the best ENL value of 1.019 in Table 4 denotes that NSST+GF efficiently eliminates speckle noise in the fetal brain ultrasound image. Nevertheless, the despeckled image appears blurry, as demonstrated in Fig. 4(c) and as indicated by the lowest AG and ALC values of 2.686 and 0.540, respectively.

NSST+MSRAD demonstrates remarkable edge preservation capabilities, as evidenced by the very high EPI value of 0.999. The despeckled image in Fig. 4(d) exhibits relatively high contrast and sharpness. These characteristics result in increased image variance, as indicated by the poorest MPSSI value and a low ENL value. However, strong edges and a low noise level contribute to achieving the best NIQE value of 3.727. Meanwhile, the application of NSST+eGDGF and NSST+eGDGF+MLV to the ultrasound image of the fetal brain generated despeckled images that exhibit the same characteristics as despeckled ultrasound images of the thyroid and breast. Speckle noise remains prominently visible in the image produced by NSST+eGDGF, as shown in Fig. 4(e). Strong contrast and many extraneous structures in the despeckled images result in suboptimal visual quality.

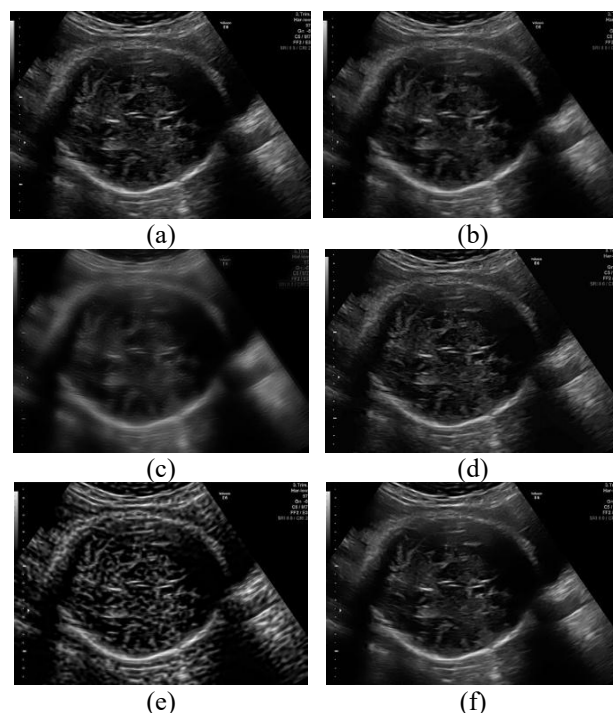


Figure. 4 The results of the despeckling of a fetal brain ultrasound image: (a) Noisy image, (b) NSST+WBF [17], (c) NSST+GF [22], (d) NSST+MSRAD [23], (e) NSST+eGDGF [37], and (f) NSST+eGDGF+MLV

Table 4. Comparison of the despeckling performance of different methods applied to a fetal brain ultrasound image

Method	ENL (↑)	MPSSI (↓)	EPI (↑)	AG (↑)	ALC (↑)	NIQE (↓)
NSST+WBF	0.782	<b>0.003</b>	0.999	5.258	2.369	4.163
NSST+GF	<b>1.019</b>	0.015	0.967	2.686	0.540	3.964
NSST+MSRAD	0.736	0.080	<b>0.999</b>	5.281	2.648	<b>3.727</b>
NSST+eGDGF	0.557	0.030	0.957	<b>6.586</b>	<b>3.121</b>	4.317
NSST+eGDGF+MLV	0.773	0.008	0.960	4.625	2.303	3.909

In contrast, NSST+eGDGF+MLV effectively reduces speckle noise while preserving edges and fine details. The contrast is sufficiently high to ensure good visual quality, as demonstrated in Fig. 4(f) and Table 4.

To further evaluate the contribution of each component in the proposed framework—namely, the eGDGF+MLV component in the LF subband and the improved thresholding shrinkage rule in the HF subbands—an ablation study was conducted. Table 5 summarizes the mean gain for six evaluation metrics. The gain of the eGDGF+MLV component was calculated by comparing the metric values of NSST+eGDGF+MLV+soft\_thresholding with the baseline (NSST+soft\_thresholding) to determine its effect on the overall performance. Meanwhile, the gain of the improved thresholding shrinkage rule was obtained by comparing NSST+improved\_thresholding with the baseline to evaluate the impact of the enhanced thresholding function. The p-value was obtained using the Wilcoxon signed-rank test with a significance level of  $\alpha < 0.05$  to assess the statistical significance of gain differences.

The analysis demonstrates that the improved thresholding shrinkage rule (H) plays a significantly greater role in improving NIQE compared to eGDGF+MLV (L). The mean gain of H (0.6106) exceeds that of L (0.2918) by about 0.3188 with p-value = 0.000414, confirming that H is the main contributor to perceptual quality enhancement. Conversely, L dominates in ENL, achieving a gain more than three times higher than H (0.01406 vs 0.00454; p-value = 0.000848), which establishes L as the primary factor in noise reduction and image smoothness improvement.

For MPSSI, H exhibits superior performance by producing a smaller increase compared to L

(-0.00033 vs -0.00520; p-value =  $1.10 \times 10^{-5}$ ), suggesting that H better preserves brightness consistency while suppressing speckle noise. In contrast, the AG analysis shows that L better preserves edge sharpness (-0.0288 vs -1.0645; p-value =  $1.08 \times 10^{-5}$ ), while in ALC, L maintains natural contrast (+0.014 vs -0.175; p-value =  $3.37 \times 10^{-5}$ ). Similarly, the EPI analysis indicates that L is the key contributor to edge preservation (-0.0014 vs -0.0484; p-value =  $1.10 \times 10^{-5}$ ), confirming that it effectively retains structural integrity.

Overall, the ablation study confirms that the L component contributes more effectively to metrics emphasizing structural preservation, contrast stability, and edge sharpness (ENL, AG, ALC, and EPI), whereas the H component excels in perceptual quality and denoising-oriented metrics (NIQE and MPSSI). Their integration provides a balanced and complementary improvement, combining the noise-suppressing capability of H with the edge- and contrast-preserving characteristics of L. Designed to operate synergistically, both components strengthen the denoising process without compromising structural fidelity, thereby achieving an optimal trade-off between speckle suppression and detail preservation.

Based on Table 6, NSST+eGDGF+MLV achieved the best overall position for the NIQE metric (1.5077), indicating the highest perceptual quality among all compared methods. This finding is reinforced by the Wilcoxon test results in Table 7, which show  $p < 10^{-12}$  against all existing approaches (NSST+WBF, NSST+GF, NSST+MSRAD, and NSST+eGDGF), with a positive decision (“+”) in every pairwise comparison. These results confirm that the perceptual quality improvements obtained by NSST+eGDGF+MLV are statistically significant.

Table 5. Average Gains for eGDGF+MLV (L) and Improved Thresholding Shrinkage Rule (H)

	NIQE	ENL	MPSSI	AG	ALC	EPI
Gain L	0.2918	0.0141	-0.0052	-0.0288	0.0141	-0.0014
Gain H	0.6106	0.0045	-0.0003	-1.0645	-0.1748	-0.0484
Gain difference	0.3188	0.0095	0.0049	1.0358	0.1889	0.0470
p-value	0.000414	0.000848	1.10E-05	1.08E-05	3.37E-05	1.10E-05

Table 6. Average Ranks

	NIQE	ENL	MPSSI	AG	ALC	EPI
NSST+WBF	<i>4.4615</i>	2.2308	<b>1.1769</b>	2.4077	3.0846	1.5154
NSST.GF	2.4923	<b>1.0231</b>	2.9846	<i>4.9846</i>	<i>4.9923</i>	3.0538
NSST.MSRAD	3.1231	3.9077	<i>4.6308</i>	2.3385	1.8846	<b>1.5077</b>
NSST.eGDGF	3.4154	<i>4.9538</i>	4.2000	<b>1.3077</b>	<b>1.3231</b>	<i>4.9615</i>
NSST.eGDGFMLV	<b>1.5077</b>	2.8846	2.0077	3.9615	3.7154	3.9615

Note: Bold values indicate the best rank, while italic values denote the worst rank.

Table 7. Wilcoxon signed-rank test results

Algorithm	NIQE		ENL		MPSSI		AG		ALC		EPI	
	p-value	Dec.	p-value	Dec.	p-value	Dec.	p-value	Dec.	p-value	Dec.	p-value	Dec.
NSST+eGDGF+MLV versus NSST+WBF	4.7E-22	+	2.7E-13	-	1.1E-17	-	4.5E-22	-	7.9E-15	-	4.5E-22	-
NSST+eGDGF+MLV versus NSST+GF	2.3E-12	+	4.5E-22	-	7.6E-17	+	4.5E-22	+	4.5E-22	+	3.5E-20	-
NSST+eGDGF+MLV versus NSST+MSRAD	2.9E-14	+	7.6E-17	+	4.5E-22	+	1.7E-21	-	1.7E-19	-	4.4E-21	-
NSST+eGDGF+MLV versus NSST+eGDGF	4.0E-20	+	4.5E-22	+	4.5E-22	+	4.5E-22	-	2.6E-21	-	6.3E-22	+

For ENL, Table 6 shows that NSST+eGDGF+MLV achieved an average rank of 2.8846, outperforming NSST+MSRAD (3.9077) and NSST+eGDGF (4.9538), with  $p\text{-value} \leq 7.6 \times 10^{-17}$ . Similarly, for MPSSI, NSST+eGDGF+MLV (2.0077) ranked better than NSST+GF (2.9846), NSST+MSRAD (4.6308), and NSST+eGDGF (4.2000), with  $p\text{-value} \leq 7.6 \times 10^{-17}$  as shown in Table 7. These findings indicate that NSST+eGDGF+MLV effectively suppresses speckle noise while maintaining the mean intensity of the image, achieving a balanced trade-off between smoothness and structural fidelity.

Regarding the AG metric, Table 6 shows that NSST+eGDGF+MLV obtained an average rank of 3.9615, superior to NSST+GF (4.9846) with a  $p\text{-value}$  of  $4.5 \times 10^{-22}$ , confirming a statistically significant difference. Although some methods with higher AG ranks may appear sharper, this sharpness often results from residual noise that amplifies false gradients. Therefore, the moderate AG value achieved by NSST+eGDGF+MLV reflects effective noise reduction without producing blurred or over-smoothed edges.

A similar trend is observed in ALC, where NSST+eGDGF+MLV achieved an average rank of 3.7154, outperforming NSST+GF (4.9923), with a  $p\text{-value}$  of  $4.5 \times 10^{-22}$ . This result confirms that the proposed method maintains local contrast at an optimal level—avoiding intensity exaggeration or flattened textures. With a moderate ALC, NSST+eGDGF+MLV produces clean, naturally contrasted images that preserve structural integrity while minimizing residual noise. For EPI, NSST+eGDGF+MLV achieved an average rank of 3.96 and showed a significant improvement over NSST+eGDGF (4.9615;  $p\text{-value} = 6.3 \times 10^{-22}$ ), highlighting that the MLV stage in low-frequency subbands enhances edge continuity and structural consistency.

Although some competing methods exhibit localized superiority in one or two metrics, NSST+eGDGF+MLV never ranks lowest in any evaluation metric, as shown in Table 6. This consistency confirms that the proposed method effectively avoids the extremes of over-smoothing and over-sharpening. The improved thresholding shrinkage rule contributes to enhanced perceptual quality through adaptive shrinkage behavior, while the eGDGF+MLV component preserves edge sharpness, contrast, and structural integrity. The synergy between these components yields statistically significant and balanced improvements across all quantitative metrics, surpassing prior approaches such as NSST+WBF, NSST+GF, and NSST+MSRAD.

The novelty of NSST+eGDGF+MLV lies in the integration of an edge-aware, contrast-preserving filter (eGDGF) with the Maximum Local Variation (MLV) operator to enhance local contrast and structural sharpness in low-frequency subbands. Meanwhile, the improved thresholding shrinkage rule is applied in high-frequency subbands to achieve adaptive speckle suppression and perceptual enhancement. This cooperative design enables effective noise reduction without sacrificing structural and perceptual fidelity, as validated by the ablation findings in Table 5 and the comparative results in Tables 6 and 7.

In order to assess the computational efficiency of the proposed framework, an analysis of runtime and memory usage was conducted. All experiments were conducted on a computer equipped with an Intel Core i5-5200U CPU (2.20 GHz) and RAM 8 GB, running Windows 10 (64-bit) with MATLAB R2017b. The performance is presented as a range rather than an average value due to the variation in resolution of the test images, which spans from  $560 \times 360$  to  $1495 \times 787$  pixels. The runtime of the proposed method varied between 41.13 s and 243.65 s, while memory usage ranged from 260 MB to 1.92 GB. These values are

higher than those of the comparative methods, which can be attributed to the additional computational load introduced by the improved thresholding shrinkage rule. Despite the longer runtime, the resulting denoised images exhibit noticeably better NIQE scores, confirming that the method achieves superior perceptual quality and visual fidelity compared with the comparative approaches.

#### 4. Conclusion

In this paper, a new ultrasound image despeckling algorithm has been proposed by combining the NSST, an enhanced gradient-domain guided filter (eGDGF) augmented with a minimum local variance (MLV) operator, and an improved thresholding shrinkage rule. The NSST employed three decomposition levels with eight shearing orientations per level to decompose the input image into one LF subband and three HF subbands. The new eGDGF+MLV was applied to the LF subband to eliminate residual noise and enhance image contrast and sharpness. Meanwhile, noise in the HF subbands was reduced using an improved shrinkage rule derived from the residual image weighted by a bilateral filter.

Experimental results demonstrate that the proposed NSST+eGDGF+MLV method achieves well-balanced despeckling performance by effectively avoiding both over-smoothing and over-sharpening. Through the integration of the eGDGF+MLV component for edge-aware, contrast-preserving enhancement and the improved thresholding shrinkage rule for adaptive speckle suppression, the algorithm delivers optimal noise reduction while maintaining structural details and enhancing the overall visual quality across ultrasound images with varying noise levels.

#### Conflicts of Interest

The authors declare no conflict of interest.

#### Author Contributions

Conceptualization, Rika Favoria Gusa and Risanuri Hidayat; methodology, Rika Favoria Gusa and Risanuri Hidayat; software, Rika Favoria Gusa; validation, Risanuri Hidayat and Hanung Adi Nugroho; formal analysis, Rika Favoria Gusa, Risanuri Hidayat and Hanung Adi Nugroho; investigation, Rika Favoria Gusa; resources, Rika Favoria Gusa; data curation, Rika Favoria Gusa; writing—original draft preparation, Rika Favoria Gusa; writing—review and editing, Rika Favoria Gusa, Risanuri Hidayat, and Hanung Adi Nugroho; visualization, Rika Favoria Gusa; supervision,

Risanuri Hidayat, and Hanung Adi Nugroho; project administration, Rika Favoria Gusa; funding acquisition, Risanuri Hidayat.

#### Acknowledgments

The authors gratefully acknowledge Universitas Gadjah Mada for financing this study under the Final Project Recognition Program (Rekognisi Tugas Akhir) for the 2025 fiscal year, as specified in letter number 4193/UN1.P1/Dit-Lit/PT.01.03/2025.

#### References

- [1] A. Koutras *et al.*, “Advantages and Limitations of Ultrasound as a Screening Test for Ovarian Cancer”, *Diagnostics*, Vol. 13, No. 13, 2023, doi: 10.3390/diagnostics13122078.
- [2] T. A. Sardjono, E. M. Yuniarno, I. M. G. Sunarya, I. K. E. Purnama, M. H. Purnomo, and N. Hermawan, “Ultrasound Probe Calibration Method of Single-Wire Phantom Using Levenberg-Marquardt Algorithm”, *Jurnal Nasional Teknik Elektro dan Teknologi Informasi*, Vol. 12, No. 3, pp. 212–218, 2023.
- [3] D. Avola, L. Cinque, A. Fagioli, G. Foresti, and A. Mecca, “Ultrasound Medical Imaging Techniques: A Survey”, *ACM Comput Surv*, Vol. 54, No. 3, 2021, doi: 10.1145/3447243.
- [4] R. F. Gusa, R. Hidayat, and H. A. Nugroho, “An Ultrasound Image Quality Improvement Approach Based on Non-Subsampled Shearlet Transform and Maximum Local Variation-Based Unsharp Masking”, In: *Proc. of the 5th International Conference on Biomedical Engineering (iBioMed 2024)*, pp. 40–45, 2024, doi: 10.1109/iBioMed62485.2024.10875811.
- [5] D. Jung, M. Kang, S. H. Park, N. Guezzi, and J. Yu, “Unsupervised speckle noise reduction technique for clinical ultrasound imaging”, *Ultrasonography*, Vol. 43, No. 5, pp. 327–344, 2024, doi: 10.14366/usg.24005.
- [6] S. V. Mohd Sagheer and S. N. George, “A review on medical image denoising algorithms”, *Biomed Signal Process Control*, Vol. 61, 2020, doi: 10.1016/j.bspc.2020.102036.
- [7] Ashpreet and M. Biswas, “Adaptive Threshold and Directional Weighted Median Filter-Based Impulse Noise Removal Method for Images”, *International Journal of Software Innovation*, Vol. 10, No. 1, pp. 1–18, 2022, doi: 10.4018/ijsi.297983.
- [8] S. Guo, G. Wang, L. Han, X. Song, and W. Yang, “COVID-19 CT image denoising algorithm based on adaptive threshold and optimized weighted median filter”, *Biomed*

- Signal Process Control*, Vol. 75, 2022, doi: 10.1016/j.bspc.2022.103552.
- [9] H. Salehi and J. Vahidi, “An Ultrasound Image Despeckling Method Based on Weighted Adaptive Bilateral Filter”, *Int J Image Graph*, Vol. 20, No. 3, 2020, doi: 10.1142/S0219467820500205.
- [10] K. Singh *et al.*, “Local Statistics-based Speckle Reducing Bilateral Filter for Medical Ultrasound Images”, *Mobile Networks and Applications*, Vol. 25, pp. 2367–2389, 2020, doi: 10.1007/s11036-020-01615-2.
- [11] G. Liu, S. Wu, Y. Shi, and X. Hua, “Guided Filter in Least Squares to Remove Non-uniform Strong Noise of Underwater Target Image”, In: *Proc. of The International Conference on Image, Vision and Intelligent Systems (ICIVIS 2021)*, pp. 551–559, 2021, doi: 10.1007/978-981-16-6963-7\_50.
- [12] B. Goyal, A. Dogra, S. Agrawal, B. S. Sohi, and A. Sharma, “Image denoising review: From classical to state-of-the-art approaches”, *Information Fusion*, Vol. 55, pp. 220–244, 2020, doi: 10.1016/j.inffus.2019.09.003.
- [13] P. Namsopa, S. Koonkarnkhai, P. Kovintavewat, H. Dinsakul, and S. Suwansawang, “A Study and Exploration of Discrete Wavelet Transform for Speckle Noise Reduction in Ultrasound Images”, In: *Proc. of 2023 International Technical Conference on Circuits/Systems, Computers, and Communications, ITC-CSCC 2023*, 2023, doi: 10.1109/ITC-CSCC58803.2023.10212853.
- [14] S. Lee and M. G. Kang, “Poisson-Gaussian noise reduction for X-ray images based on local linear minimum mean square error shrinkage in nonsubsampling contourlet transform domain”, *IEEE Access*, Vol. 9, pp. 100637–100651, 2021, doi: 10.1109/ACCESS.2021.3097078.
- [15] A. Goel and A. Garg, “Despeckling Of Synthetic Aperture Radar Images Using Shearlet Transform”, *Advances in Electrical and Electronic Engineering*, Vol. 21, No. 3, pp. 245–257, 2023, doi: 10.15598/aece.v21i3.4814.
- [16] S. Routray, P. P. Malla, S. K. Sharma, S. K. Panda, and G. Palai, “A new image denoising framework using bilateral filtering based non-subsampling shearlet transform”, *Optik (Stuttg)*, Vol. 216, 2020, doi: 10.1016/j.ijleo.2020.164903.
- [17] P. Singh, M. Diwakar, S. Singh, S. Kumar, A. Tripathi, and A. Shankar, “A homomorphic non-subsampling contourlet transform based ultrasound image despeckling by novel thresholding function and self-organizing map”, *Biocybern Biomed Eng*, Vol. 42, No. 2, pp. 512–528, 2022, doi: 10.1016/j.bbe.2022.03.003.
- [18] A. E. Ilesanmi, O. P. Idowu, U. Chaumrattanakul, and S. S. Makhanov, “Multiscale hybrid algorithm for pre-processing of ultrasound images”, *Biomed Signal Process Control*, Vol. 66, 2021, doi: 10.1016/j.bspc.2020.102396.
- [19] T. Joel and R. Sivakumar, “Nonsubsampling contourlet transform with cross-guided bilateral filter for despeckling of medical ultrasound images”, *Int J Imaging Syst Technol*, Vol. 31, No. 2, pp. 763–777, 2020, doi: 10.1002/ima.22502.
- [20] L. Jubairahmed, S. Satheeskumaran, and C. Venkatesan, “Contourlet transform based adaptive nonlinear diffusion filtering for speckle noise removal in ultrasound images”, *Cluster Comput*, Vol. 22, pp. 11237–11246, 2019, doi: 10.1007/s10586-017-1370-x.
- [21] J. Zhang, X. Xiu, J. Zhou, K. Zhao, Z. Tian, and Y. Cheng, “A Novel Despeckling Method for Medical Ultrasound Images Based on the Nonsubsampling Shearlet and Guided Filter”, *Circuits Syst Signal Process*, Vol. 39, No. 3, pp. 1449–1470, 2020, doi: 10.1007/s00034-019-01201-2.
- [22] A. K. Bedi, R. K. Sunkaria, and D. Mittal, “Ultrasound Image Despeckling and Enhancement using Modified Multiscale Anisotropic Diffusion Model in Non-Subsampling Shearlet Domain”, *Comput J*, Vol. 64, No. 12, pp. 1785–1800, 2021, doi: 10.1093/comjnl/bxzl131.
- [23] Z. Lyu, Y. Chen, Y. Hou, and C. Zhang, “NSTBNet: Toward a nonsubsampling shearlet transform for broad convolutional neural network image denoising”, *Digital Signal Processing: A Review Journal*, Vol. 123, 2022, doi: 10.1016/j.dsp.2022.103407.
- [24] S. Katta, P. Singh, D. Garg, V. Ravi, and M. Diwakar, “A Dual CT Image Denoising Approach Using Guided Filter and Method-Based Noise in the NSST Domain”, *Open Bioinforma J*, Vol. 18, No. 1, 2025, doi: 10.2174/0118750362370719250411094442.
- [25] Y. Sun, Z. Huang, G. Cai, J. Su, and Z. Gong, “NSBR-Net: A Novel Noise Suppression and Boundary Refinement Network for Breast Tumor Segmentation in Ultrasound Images”, *Algorithms*, Vol. 17, 2024, doi: 10.3390/a17060257.
- [26] H. Kang, C. Park, and H. Yang, “Evaluation of Denoising Performance of ResNet Deep Learning Model for Ultrasound Images

- Corresponding to Two Frequency Parameters”, *Bioengineering*, Vol. 11, No. 7, 2024, doi: 10.3390/bioengineering11070723.
- [27] M. Khalifa, H. M. Hamza, and K. M. Hosny, “De-speckling of medical ultrasound image using metric-optimized knowledge distillation”, *Sci Rep*, Vol. 15, No. 1, 2025, doi: 10.1038/s41598-025-07115-1.
- [28] C. Yu, F. Ren, S. Bao, Y. Yang, and X. Xu, “Self-supervised ultrasound image denoising based on weighted joint loss”, *Digital Signal Processing: A Review Journal*, Vol. 162, 2025, doi: 10.1016/j.dsp.2025.105151.
- [29] G. Easley, D. Labate, and W. Q. Lim, “Sparse directional image representations using the discrete shearlet transform”, *Appl Comput Harmon Anal*, Vol. 25, No. 1, pp. 25–46, 2008, doi: 10.1016/j.acha.2007.09.003.
- [30] A. Morteza and M. Amirmazlaghani, “A novel statistical approach for multiplicative speckle removal using t-locations scale and non-sub sampled shearlet transform”, *Digital Signal Processing: A Review Journal*, Vol. 107, 2020, doi: 10.1016/j.dsp.2020.102857.
- [31] F. Kou, W. Chen, C. Wen, and Z. Li, “Gradient Domain Guided Image Filtering”, *IEEE Transactions on Image Processing*, Vol. 24, No. 11, pp. 4528–4539, 2015, doi: 10.1109/TIP.2015.2468183.
- [32] Z. Li, H. Liu, L. Cheng, and X. Jia, “Image Denoising Algorithm Based on Gradient Domain Guided Filtering and NSST”, *IEEE Access*, Vol. 11, pp. 11923–11933, 2023, doi: 10.1109/ACCESS.2023.3242050.
- [33] S. G. Chang, B. Yu, and M. Vetterli, “Adaptive Wavelet Thresholding for Image Denoising and Compression”, *IEEE Transactions on Image processing*, Vol. 9, No. 9, pp. 1532–1546, 2000.
- [34] L. Pedraza, C. Vargas, F. Narváez, O. Durán, E. Muñoz, and E. Romero, “An open access thyroid ultrasound image database”, In: *Proc. of 10th International Symposium on Medical Information Processing and Analysis, Cartagena de Indias, Colombia: SPIE*, 2015, p. 92870W. doi: 10.1117/12.2073532.
- [35] W. Al-Dhabyani, M. Gomaa, H. Khaled, and A. Fahmy, “Dataset of breast ultrasound images”, *Data Brief*, Vol. 28, p. 104863, 2020, doi: 10.1016/j.dib.2019.104863.
- [36] X. P. Burgoz-Artizzu *et al.*, “Evaluation of deep convolutional neural networks for automatic classification of common maternal fetal ultrasound planes”, *Sci Rep*, Vol. 10, 2020.
- [37] T. Zhao and S.-X. Zhang, “X-ray Image Enhancement Based on Nonsampled Shearlet Transform and Gradient Domain Guided Filtering”, *Sensors*, Vol. 22, No. 4074, 2022.
- [38] S. G. Dellepiane and E. Angiati, “Quality assessment of despeckled SAR images”, *IEEE J Sel Top Appl Earth Obs Remote Sens*, Vol. 7, No. 2, pp. 691–707, 2014, doi: 10.1109/JSTARS.2013.2279501.
- [39] F. Sattar, L. Floreby, G. Salomonsson, and B. Lovstrom, “Image Enhancement Based on a Nonlinear Multiscale Method”, *IEEE Transactions on Image Processing*, Vol. 6, No. 6, pp. 888–895, 1997.
- [40] R. F. Gusa, R. Hidayat, and H. A. Nugroho, “Performance Analysis of Enhancement Methods on Fetal Ultrasound Images”, In: *Proc. of the 2023 IEEE International Conference on Industry 4.0, Artificial Intelligence, and Communications Technology*, pp. 326–331, 2023, doi: 10.1109/IAICT59002.2023.10205792.
- [41] A. Mittal, R. Soundararajan, and A. C. Bovik, “Making a ‘Completely Blind’ Image Quality Analyzer”, *IEEE Signal Process Lett*, Vol. 20, No. 3, pp. 209–212, 2013, doi: 10.1109/LSP.2012.2227726.